Experimentally-guided *in silico* design of engineered heart tissues to improve cardiac electrical function after myocardial infarction

Ricardo M. Rosales [a,b,c,*], Konstantinos A. Mountris [d], Aida Oliván-Viguera [a,b,c],
María Pérez-Zabalza [a,b,c,e], Gerardo Cedillo-Servin [f,g], Olalla Iglesias-García [h,i],
Andrei Hrynevich [f,g], Miguel Castilho [g,j], Jos Malda [f,g,k], Felipe Prósper [h,i,l,m], Manuel Doblaré [a,b,c],
Manuel M. Mazo [h,i,l], Esther Pueyo [a,b,c]

[a] *Instituto de Investigación Sanitaria de Aragón (IIS Aragón), Zaragoza, Aragón, Spain*
[b] *CIBER-BBN, ISCIII, Madrid, Spain*
[c] *Aragón Institute of Engineering Research (I3A), University of Zaragoza, Zaragoza, Aragón, Spain*
[d] *Department of Mechanical Engineering, University College London, London, United Kingdom*
[e] *Defense University Centre (CUD), Zaragoza, Spain*
[f] *Regenerative Medicine Center, Utrecht, The Netherlands*
[g] *Department of Orthopedics, University Medical Center, Utrecht, The Netherlands*
[h] *Regenerative Medicine Program, CIMA Universidad de Navarra, Pamplona, Spain*
[i] *Instituto de Investigación Sanitaria de Navarra (IdiSNA), Spain*
[j] *Department of Biomedical Engineering, Eindhoven University of Technology, Eindhoven, The Netherlands*
[k] *Department of Equine Sciences, Faculty of Veterinary Medicine, Utrecht University, Utrecht, The Netherlands*
[l] *Hematology and Cell Therapy, Clínica Universidad de Navarra, Pamplona, Spain*
[m] *CIBER de Cáncer (CIBERONC, team CB16/12/00489), Pamplona, Spain*

ARTICLE INFO

ABSTRACT

Engineered heart tissues (EHTs) built from human induced pluripotent stem cell-derived cardiomyocytes (hiPSC-CMs) showed promising results for cardiac function restoration following myocardial infarction. Nevertheless, human iPSC-CMs have longer action potential and lower cell-to-cell coupling than adult-like CMs. These immature electrophysiological properties favor arrhythmias due to the generation of electrophysiological gradients when hiPSC-CMs are injected in the cardiac tissue. Culturing hiPSC-CMs on three-dimensional (3D) scaffolds can promote their maturation and influence their alignment. However, it is still uncertain how on-scaffold culturing influences the overall electrophysiology of the *in vitro* and implanted EHTs, as it requires expensive and time consuming experimentation. Here, we computationally investigated the impact of the scaffold design on the EHT electrical depolarization and repolarization before and after engraftment on infarcted tissue. We first acquired and processed electrical recordings from *in vitro* EHTs, which we used to calibrate the modeling and simulation of *in silico* EHTs to replicate experimental outcomes. Next, we built *in silico* EHT models for a range of scaffold pore sizes, shapes (square, rectangular, auxetic, hexagonal) and thicknesses. In this setup, we found that scaffolds made of small (0.2 mm^2), elongated (30° half-angle) hexagons led to faster EHT activation and better mimicked the cardiac anisotropy. The scaffold thickness had a marginal role on the not engrafted EHT electrophysiology. Moreover, EHT engraftment on infarcted tissue showed that the EHT conductivity should be at least 5% of that in healthy tissue for bidirectional EHT-myocardium electrical propagation. For conductivities above such threshold, the scaffold made of small elongated hexagons led to the lowest activation time (AT) in the coupled EHT-myocardium. If the EHT conductivity was further increased and the hiPSC-CMs were uniformly oriented parallel to the epicardial cells, the total AT and the repolarization time gradient decreased substantially, thus minimizing the likelihood for arrhythmias after EHT transplantation.

* Corresponding author at: Instituto de Investigación Sanitaria de Aragón (IIS Aragón), Zaragoza, Aragón, Spain.
E-mail addresses: rrosales@unizar.es (R.M. Rosales), k.mountris@ucl.ac.uk (K.A. Mountris), aolivanv@unizar.es (A. Oliván-Viguera),
mariapzabalza@unizar.es (M. Pérez-Zabalza), g.cedilloservin@umcutrecht.nl (G. Cedillo-Servin), oiglesias@unav.es (O. Iglesias-García),
a.hrynevich@umcutrecht.nl (A. Hrynevich), m.dias.castilho@tue.nl (M. Castilho), j.malda@umcutrecht.nl (J. Malda), fprosper@unav.es (F. Prósper),
mdoblare@unizar.es (M. Doblaré), mmazoveg@unav.es (M.M. Mazo), epueyo@unizar.es (E. Pueyo).

1. Introduction

Myocardial infarction (MI) is the leading cause of mortality worldwide, standing behind 45% and 39% of female and male deaths respectively during 2021 [1]. Even if the improvement in treatment strategies has made most patients to survive acute MI, there is a subsequent induced pathological remodeling that has major impact on patient outcomes. The remodeling involves progressive cardiomyocyte death, the formation of a fibrotic scar and impairments in the diastolic and systolic heart function [2]. All these alterations following MI increase the risk for heart failure and enhance vulnerability to arrhythmias and sudden cardiac death [2,3].

In recent years, novel treatment strategies have been developed that involve the repopulation of MI-injured myocardial regions with human induced pluripotent stem cell-derived cardiomyocytes (hiPSC-CMs). By integration and proliferation of the hiPSC-CMs in the MI region, these strategies aim at recovering cardiac function. They, thus, represent promising alternatives to current solutions, such as cardiac transplantation and left ventricular assist devices [4,5]. Heart transplantation is a highly complex surgical procedure, only considered in some cases of end-stage heart failure, as its main shortcoming is the lack of availability of human donors. Once a donor-recipient match has been identified after an exhaustive analysis of their risk factors, many complications still need to be overcome for this technique to provide long-term patient survival, with some of the main complications being related to graft dysfunction and failure, life-long immunosuppression, allograft rejection and cardiac allograft vasculopathy [6]. Regarding left ventricular assist devices, they usually represent a temporal therapy while waiting for heart transplantation and their implantation involves cumbersome invasive surgeries and the administration of long-term anticoagulation drugs [4,5].

An important limitation of the use of hiPSC-CMs is their lack of maturation. The structural, electrical, mechanical and metabolic immaturity of these fetal-like cells is the result of the notable shortfall of transverse tubules, mature calcium handling and oxidative metabolism [7]. Mechanically, structural deficiencies such as sarcomere length and organization can originate contractions with short amplitude and duration that might be insufficient to restore cardiac function. Electrically, immature hiPSC-CMs present spontaneous electrical activity, higher diastolic membrane potential, longer action potentials and lower upstroke velocity than adult CMs. These dissimilarities unleash electrophysiological heterogeneities that could increase the risk for arrhythmias when transplanting hiPSC-CMs into the host tissue [4,8].

The lack of maturation has been suggested to originate as a consequence of hiPSC-CMs culturing in non-biomimetic milieus in absence of stromal and vascular cardiac cells and the biophysical interactions among them [8]. Therefore, electrical and mechanical stimulation, topographical and chemical substrates and other tissue engineering techniques have been investigated to generate cells more closely mimicking adult-like CMs. Recent studies have postulated that maturation can be promoted by culturing cells in engineered patches [9–12]. Modern additive manufacturing techniques, such as melt electrowriting (MEW), are able to build scaffolds resembling the extracellular matrix [13]. Nevertheless, a thorough characterization of the conduction and repolarization properties of hiPSC-CMs cultured in those scaffolds is yet lacking, which could help to identify the optimal culturing conditions to provide engineered heart tissues (EHTs) able to recover cardiac function while not exacerbating arrhythmic risk when engrafted on the infarcted myocardium.

In the past decades, the use of computational modeling and simulation has grown exponentially with the aid of drastic improvements in computational resources and experimental data collection. *In silico* models now enable highly detailed representations of biological processes and contribute to reduce expensive and time consuming experimental trials. Ionic, cell, tissue and whole-organ *in silico* models can be employed to e.g. evaluate spatiotemporal distributions of electrophysiological variables or to assess therapeutic interventions [14,15]. It is currently feasible to investigate the effects of engrafting EHTs in ventricular tissues after MI with the aid of *in silico* simulations of cardiac electrical activity.

This work aims to *in silico* determine the scaffold characteristics that render EHTs closely replicating the electrophysiology of healthy heart tissue. First, an initial model calibration is performed based on the acquisition and processing of *in vitro* electrical recordings acquired from EHTs manufactured with the MEW technique and loaded with hiPSC-derived cells. We build a linear model between the electrical conductivity, represented by the longitudinal diffusion coefficient (LDC), and the cellular alignment (CA) in the *in silico* EHT models according to the experimental results. Once the CA-conductivity relation was defined, a comprehensive evaluation of the depolarization and repolarization properties of the EHTs is conducted for scaffolds created using different thicknesses and a range of pore shapes and sizes. Subsequently, *in silico* EHTs are engrafted on three-dimensional (3D) slabs composed of healthy and infarcted tissues. Activation time (AT), conduction velocity (CV) and repolarization time (RT) gradient (RTG) are calculated to assess propagation and arrhythmic risk in the coupled EHT-myocardium.

A preliminary version of this work was reported in [16]. Substantial additions were included in the present manuscript with respect to [16]. These include experimental analysis of more complex pore-shaped EHTs, novel numerical simulations with improved EHT models based on an extended *in vitro* acquisition and processing of electrical recordings as well as more accurate definition of *in silico* model parameters based on experimental evidence. Also, we extended our previous *in silico* evaluation of EHT designs by adding different scaffold's pore shapes, by including variations on scaffold's pore size and by varying overall EHT thickness, maturation-related conductivity and CA. Importantly, here we tested electrophysiological changes generated by different EHT designs not only before but also after the EHTs were engrafted on slabs of infarcted ventricular tissue. Furthermore, we performed a new arrhythmic risk assessment based not only on ATs but also on CVs for the individual EHT models (not coupled to cardiac tissue), and on ATs, CVs and RTGs for the *in silico* coupled EHT-myocardium models. Thus, a more exhaustive and robust evaluation is presented in the present study that considers a wider number of variables and simulation cases and allows to more thoroughly and realistically characterize the electrical propagation in EHTs, both alone and when engrafted on infarcted myocardium.

2. Methodology

Fig. 1 depicts the four main tasks conducted in this work, one experimental task described in Section 2.1 and three *in silico* tasks described in Sections 2.2.2–2.2.4. First, we acquired and analyzed electrophysiological data obtained from *in vitro* EHTs (Fig. 1a). Next, we *in silico* replicated this experimental data (Fig. 1b) by adjusting the model parameters. Subsequently, we *in silico* assessed the electrophysiological behavior of distinct EHT designs both before and after being implanted on a slab of MI tissue (Fig. 1c and d, respectively).

2.1. Experimental electrophysiological analysis of in vitro EHTs

2.1.1. Experimental data acquisition

Electrophysiological recordings from a two-dimensional (2D) scaffold-free culture and four 3D scaffold-based EHTs were acquired and processed. Three different recordings were collected for each of the EHTs and one recording was collected for the 2D control culture, which rendered 13 electrical recordings for analysis. The results of the electrical propagation analysis served as a basis to evaluate the impact of the scaffold used to culture hiPSC-CMs. In particular, the alignment and maturation of hiPSC-CMs, which have been reported to be lower
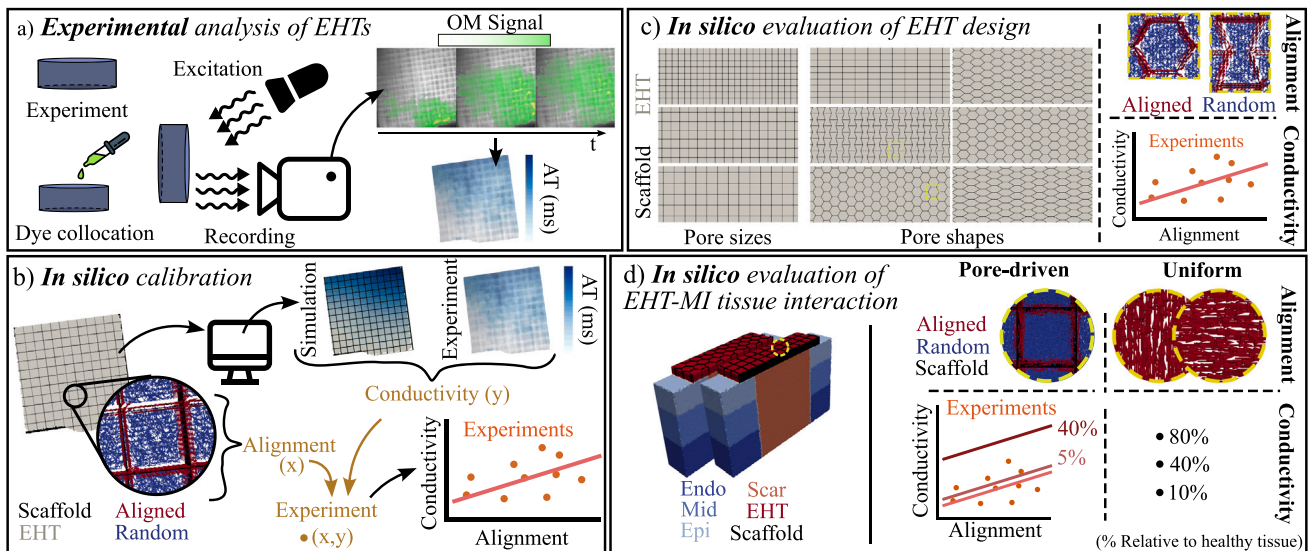
Fig. 1. Experimental and *in silico* assessment. (a) Experimental data acquisition by optical mapping and resulting AT map for a square-pore EHT. (b) *In silico* calibration of EHT models, with illustration of the comparison between experimental and simulated ATs and the derived CA-conductivity relation. (c) *In silico* evaluation of EHT designs by electrophysiological analysis of different scaffold's pore sizes and shapes (left panel) and its definition of CA and conductivity (right panel). (d) *In silico* evaluation of EHTs engrafted on a slab of MI tissue (left panel) and the pore-driven and uniform approaches used for defining CA and electrical conductivity in the engrafted EHT (right panel).

for 2D scaffold-free cultures than 3D EHTs [17], were considered as a function of the scaffold characteristics.

For EHTs, fiber scaffolds were printed in medical grade poly-ε-caprolactone (mPCL, Purasorb PC 12, Corbion) using a purpose-built MEW device (QUT, Queensland, Australia). Of the 4 EHTs, 3 had square pores and 1 had regular hexagonal pores. All 2D and 3D experiments had a surface area of 5×5 mm^2 and, in the 3D cases, a thickness of 0.2 mm. The pore area was 0.04 and 0.42 mm^2 for square and hexagonal geometries, respectively. Human iPSC-derived cells were produced in-house as described in [17] and embedded in growth factor reduced matrigel and fibrin for the square and hexagonal pore-shaped EHTs, respectively. Both hydrogels were expected to provide only a transient support and to quickly degrade, thus not interfering with cellular communication. The hexagonal pore EHT was made available from an ongoing investigation assessing culturing hydrogels and it contained 10% of hiPSC-derived cardiac fibroblasts (hiPSC-CFs). The hydrogel-cells complexes were casted on the printed scaffolds, with similar cellular densities for all EHTs, and were cultured for 28 days. For the 2D culture, cells were plated on slide chambers (Ibidi).

High temporal and spatial resolution videos of Ca^{2+} transient activity in the EHTs were acquired by optical mapping (OM) employing a MiCAM O5-Ultima CMOS camera (SciMedia, Costa Mesa, CA). Samples were stained by immersion in culture medium supplemented with Rhod-2 AM (Ca^{2+} sensitive dye, Invitrogen, Eugene, OR) at 5 μM for 30 min under incubation conditions (37 °C, 5% CO$_2$). Blebbistatin (10 μM, Tocris Bioscience, St. Louis, MO) incubation during 30 min prevented motion artifacts. Ca^{2+} transients were acquired due to the increased recorded fluorescence amplitude associated with Ca^{2+} dyes compared to voltage dyes. After dye incubation, the EHTs were placed in a heated chamber (RC-27NE in a PM-6 heated platform, Warner Instruments) at 36.5 °C with 1 mL pre-oxygenated Tyrode's solution (supplemented with 30 mM BDM to prevent motion artifacts) and Ca^{2+} concentration was mapped. EHTs were excited using a high intensity LED illumination system through an excitation filter of 530 nm (LEX2-LZ4, SciMedia, Costa Mesa, CA, USA). Emitted fluorescence was collected through a THT-macroscope (SciMedia) and detected with a camera equipped with a 575/15 nm band-pass filter. A sampling frequency of 500 Hz and a spatial resolution of 100×100 pixels per frame, with a field of view of 3.1 mm, were used. The EHTs were field-stimulated with two platinum electrodes at 1 and 2 Hz [18], using an A385 stimulator (World Precision Instruments, Sarasota, FL) to apply monopolar pulses

of 70 mA amplitude and 3 ms duration. After a short stimulation period to allow the EHTs to adjust to the pacing rate, 20-s recordings were acquired.

2.1.2. Experimental data processing

Optical mapping signals were analyzed using custom-written software [19]. A region of interest was manually defined for each mapped EHT. Baseline drift in the signals was attenuated by high-pass filtering with a cut-off frequency of 0.4 Hz. High-frequency noise was removed by using an adaptive spatio-temporal Gaussian filter with automatic selection of its parameter values as a function of the recording characteristics [19,20]. Fig. 2(b) presents the Ca^{2+} signals corresponding to the points X_a and X_b marked in the EHT of Fig. 2(a), which were obtained after application of the described processing and subsequent normalization. From the individual signals, denoted by $x_i(t)$, $i = 1, \ldots, N$, with N the total number of pixels in the region of interest, a mean Ca^{2+} signal, $\overline{x}(t)$, was calculated by first aligning the signals and subsequently averaging them. Cross-correlation between each individual signal $x_i(t)$ and the mean signal $\overline{x}(t)$ was computed and only those individual signals with maximum correlation above 0.86 were used for subsequent analysis. Next, local ATs were calculated for each $x_i(t)$, $i = 1, \ldots, N$, as exemplified in Fig. 2(e). Specifically, the AT value for $x_i(t)$ and a given beat was computed as the time elapsed between a fixed time reference, denoted by A, and the time associated with the maximum derivative of $x_i(t)$ in that beat, denoted by U. The reference A was defined from the mean signal $\overline{x}(t)$ in the given beat by subtracting a constant B to the time C associated with the maximum $\overline{x}(t)$ value. Thus, a unique reference A was set for AT calculation in all pixels. A final AT value was computed for each pixel as the median of the ATs of all beats.

As depicted in Fig. 2(a), an AT map was obtained from the ATs of all pixels. Image processing techniques, including opening, closing and median filtering operations, were applied to remove isolated clusters of cells. The AT values from all pixels were clustered with a dendrogram based on the Euclidean distance among cluster centroids, as illustrated in Fig. 2(c). This served to visually assess depolarization propagation and to define the stimulation region when using *in silico* models (see Section 2.2.5).
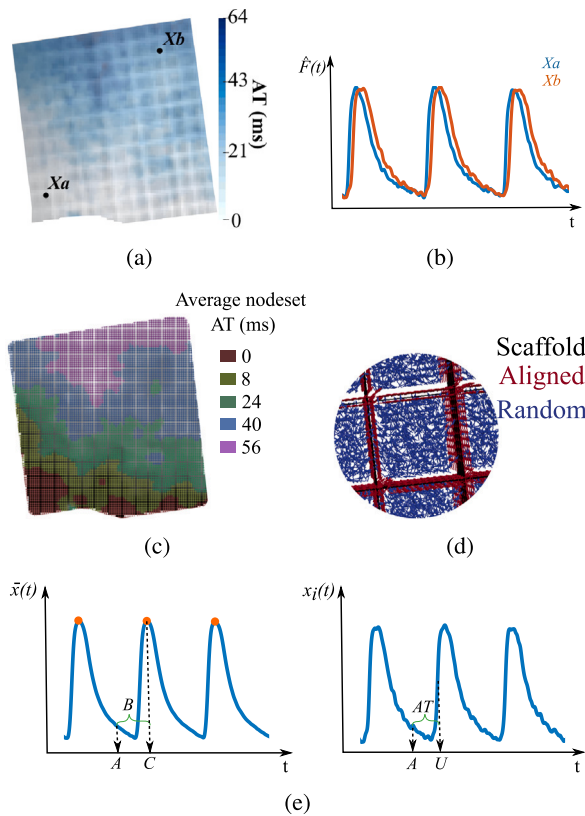
Fig. 2. (a) Experimental AT map. (b) Normalized OM signals for points X_a and X_b. (c) *In silico* mesh generation and node set definition. (d) Tissue node alignment, with red and blue arrows representing aligned and random orientations, respectively. (e) AT calculation for an individual action potential. *A* is the time reference computed from the time of peak *C* of the average EHT action potential, $\bar{x}(t)$, minus a predefined distance *B*. The time *U* corresponds to the maximum derivative of the action potential upstroke for the individual signal $x_i(t)$. AT is the time difference between A and U.

2.2. In silico electrophysiological analysis of EHTs

2.2.1. Cellular alignment and conductivity of in silico models

Three sets of computational simulations were conducted, as shown in Fig. 1b–d. Both pore-driven and uniform approaches were used to define the CA and conductivity values in the *in silico* analysis. The CA was defined as:

- **Pore-driven:** hiPSC-CMs located in the center of the scaffold pore were set to be randomly aligned, while the hiPSC-CMs near the pore walls were oriented following the pore wall direction, as observed experimentally [17].
- **Uniform:** all hiPSC-CMs in the EHT were oriented either randomly or following a unique direction.

The conductivity was defined as:

- **Pore-driven:** the LDC was defined based on the percentage of CA associated with the scaffold architecture. Specifically, each *in vitro* EHT experiment was represented by an *in silico* model and the percentage of pore-driven CA was paired to the *in silico* LDC required to replicate the maximum AT in the experiment. All the CA-LDC pairs were fitted using a linear function, which allowed setting the EHT conductivity for any EHT design.
- **Uniform:** the conductivity in the EHT was set to a constant value, which was made relative to the conductivity in the healthy myocardium.

Table 1
CA and conductivity values used in each set of *in silico* simulations. The offset percentage applies to the linear CA-conductivity relation and it is relative to the conductivity in the healthy myocardium.

Case	CA	Conductivity
Experimental replication	Pore-driven	Determined
Not engrafted EHT designs	Pore-driven	Pore-driven
Engrafted EHT designs	Pore-driven	Pore-driven (5% offset)
	Pore-driven	Pore-driven (40% offset)
	Uniform	Uniform

Table 1 presents a summary of CA and conductivity definitions for each of the three sets of *in silico* simulations. The following sections describe the modeling and simulation in each of the three sets and present the methods used to run the simulations and compute the electrophysiological markers derived from those simulations.

2.2.2. In vitro-based construction of in silico EHT models

In silico scaffold-free and scaffold-based models were built. For calibration purposes, we generated *in silico* scaffold meshes that allowed reproducing the experimental results described in Section 2.1.2. Square pore-shaped scaffold meshes were automatically constructed from the corresponding experimental images. For the hexagonal pore-shaped scaffold, experimental images showed substantial deformation associated with contraction-relaxation cycles prior to its inhibition with blebbistatin. This deformation was significantly more accentuated in the hexagonal pore-shaped scaffolds due to their lower stiffness compared to square pore-shaped scaffolds [10]. Therefore, a semiautomatic approach was developed to generate the *in silico* meshes. This included threshold and manual segmentation in combination with skeletonization to determine the scaffold profile from microscopical images. The *in silico* meshes were defined from the skeleton's binary images. The scaffold wall directions were subsequently identified.

The *in silico* EHT models were built by assembling the *in silico* scaffold meshes with coupled hiPSC-CMs. The spatial resolution of these models was fixed at 31 μm, which agrees with the pixel resolution of the OM experiments. The spatial discretization was implemented using quadrilateral and hexahedral elements for 2D and 3D models, respectively. For the 2D scaffold-free model, CA for every node of the tissue was assigned from a uniform statistical distribution spanning 0–180 degrees in plane. For 3D scaffold-based EHT models, tissue nodes within a distance of 27 μm to the scaffold were assigned to a CA according to the direction of the pore walls, as depicted in Fig. 2(d). This distance threshold was chosen in agreement with experimental measures reported in the literature [10,17]. The CA assigned for every other node far from the scaffold was extracted from an uniform random distribution, as in the 2D scaffold-free case. The CA along the thickness was kept constant due to the lack of accurate experimental information.

Conductivity was considered to be orthotropic with transverse isotropy, i.e. with equal sheet and normal-sheet conductivities. A transverse-to-longitudinal conductivity ratio of 0.25 was used, which led to conduction velocity anisotropy in agreement with that reported for cardiac tissue [21]. As mentioned, the LDC was adjusted so that the maximum AT values in the simulations of square and hexagonal pore-shaped EHTs matched the corresponding experimental AT values calculated as described in Section 2.1.2.

To extrapolate the LDC values to EHT designs other than those used for model calibration, the data representing the relationship between conductivity and CA for all experimentally-based simulations were fitted with a linear polynomial using a least-square criterion. The percentage of CA was calculated by dividing the number of tissue nodes aligned to the scaffold fibers by the total number of nodes.
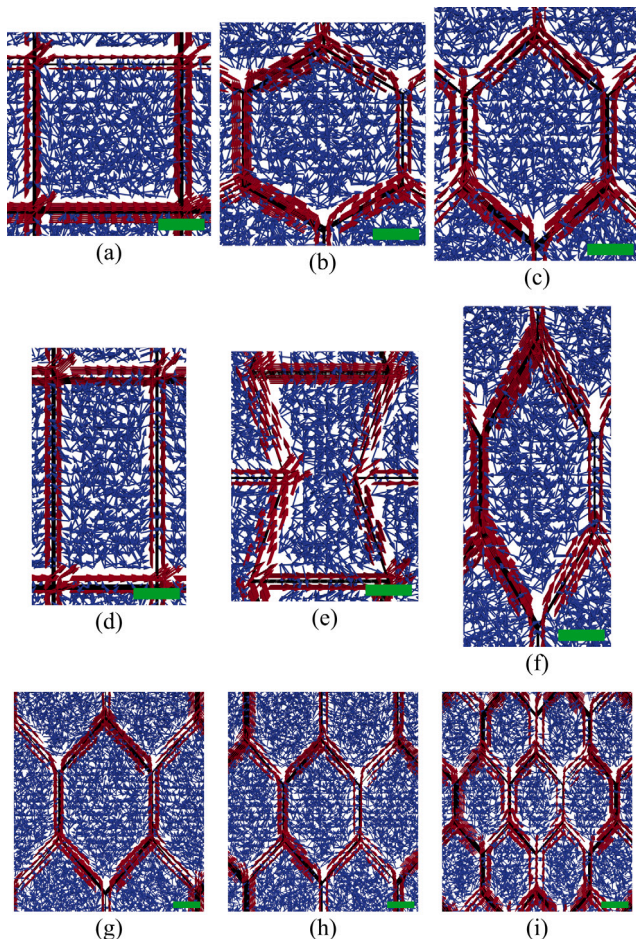
Fig. 3. EHT pore architectures and fiber alignments: (a) square, (d) rectangle, (e) auxetic, (b), (c) and (f) hexagonal with 60°, 50° and 30° half angles and 0.4 mm² area; (g), (h) and (i): 40° half-angle hexagons with 0.6, 0.4 and 0.2 mm² area. Red and blue arrows represent aligned and random orientations, respectively, while black lines depict the scaffold's pore walls. The length of the green scale bars is 0.2 mm.

Fig. 4. *In silico* model of an EHT engrafted on a slab of infarcted myocardial tissue. (a) Myocardial tissue and EHT mesh. (b) The CA of the myocardial tissue and the EHT cultured in a square pore-shaped scaffold.

2.2.3. In silico testing of scaffold designs for EHTs

Once model conductivity values were set based on the calibration described in Section 2.2.2, additional EHTs were built to assess the impact of variations in scaffold pore geometry and size and in scaffold thickness.

Scaffold pore shapes included square, rectangle, hexagons with half angles of 60°, 50°, 40° and 30°, and auxetic architectures perpendicular and parallel to the depolarizing direction. The 3D EHTs with all these pore geometries were tested for 0.2, 0.4 and 0.6 mm² pore areas, as shown in Fig. 3g–i for the 40° elongated hexagon. Only the 0.4 mm² pore area was studied for 2D scaffold-based EHTs.

Rectangular tissue meshes of 4 × 10 mm² were generated for 2D EHTs. For 3D EHTs, tissue meshes of the same surface size with a thickness of 0.2 mm were built. This thickness enhanced cell viability compared to larger thicknesses [22]. The tissue model was discretized with 50 μm-side square and hexahedral elements for 2D and 3D cases, respectively [23].

Scaffold meshes were built covering the corresponding tissue. The scaffold and tissue centroid positions were matched and tissue nodes CA was defined according to the scaffold wall directions, as described in Section 2.2.2. To emphasize the effect of the scaffold's pore structure, a higher distance threshold of 55 μm was used to define tissue nodes CA (Fig. 3).

The LDC was computed as a function of the CA percentage according to the linear relationship established in Section 2.2.2. To further describe the effect of the scaffold's characteristics on electrical activation
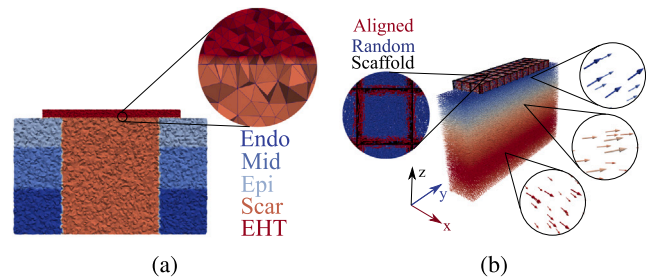
while taking into account that the scaffold walls may orient cells transverse to the propagating wavefront, we additionally calculated a longitudinal cellular alignment (LCA) metric different from the CA metric. The LCA metric was defined as the percentage of tissue nodes oriented within ± 45° from the overall depolarization direction.

Next, we modeled variations in the EHT thickness by varying it from 0.2 to 0.6 mm, with the surface area of the tissue set at 3 × 6 mm². The spatial resolution was equal to 50 μm in the three dimensions, as in the above described tests. The scaffold size matched the tissue size, with a 0.2 mm-side square pore. The CA was set using a distance threshold of 27 μm and the LDC was obtained from the linear relationship established in Section 2.2.2.

2.2.4. In silico models coupling EHTs and infarcted tissues

The EHT models of previous sections were coupled to a slab of myocardial tissue. Fig. 4 shows an example of an *in silico* transmural tissue slab of healthy and infarcted tissue with a size of 2 × 10 × 6 mm³ on which a 2 × 7 × 0.5 mm³ EHT was engrafted. The myocardial thickness was chosen based on the human ventricular wall size [24]. The EHT thickness was representative of modern MEW-based scaffolds [10]. The integrated EHT-myocardium mesh was discretized with 702 486 irregular tetrahedrons interconnecting 125 202 nodes. The mean edge length of the mesh was 120 and 50 μm for the myocardial and EHT regions, respectively. Transmural heterogeneities were represented by assigning 40%, 35% and 25% of the nodes with endo-, mid- and epicardial cell properties. A scar of 2 × 5 × 6 mm³ was positioned in the center of the tissue slab to model a chronic transmural MI.

Orthotropic conductivity with transverse isotropy was considered for the myocardial tissue and the EHT. The LDC in the myocardium was set to 0.0013 cm²/ms (equivalent to 0.13 S/m for a membrane surface-to-volume ratio of 1000 cm⁻¹ and capacitance per unit area of 1 μF/cm²) and the scar was defined as a non-conducting region. The LDC and CA in the EHT were set as pore-driven or uniform, as described in Section 2.2.1. In the pore-driven approach, a distance threshold of 55 μm for the cells with respect to the scaffold walls was used for computing the CA metric. If the calculated EHT LDC was below 1% of that in the healthy myocardium, a 5% offset was added to avoid conduction block at the EHT. For both the myocardial tissue and the EHT, the transverse-to-longitudinal conductivity ratio was set to 0.25.

The CA in the myocardium was linearly varied in a 120° range from epi- to endocardium. The EHT was oriented in three different ways, representing the EHT being parallel and perpendicular to the epicardial CMs and parallel to the left ventricle long axis. This was equivalent to the epicardial cells being oriented with angles of 0°, 90° and 60° from the longitudinal direction of the EHT. Since similar electrophysiological outcomes were obtained for different pore shapes with a common area of 0.4 mm² when the three different EHT alignments were tested, the following analyses were only performed with the overall EHT architecture being aligned parallel to the epicardial CMs.

As shown in Table 1, three groups of numerical simulations were conducted to evaluate electrophysiological changes when the EHT was

engrafted on the infarcted tissue slab. In the first group (G1), we tested different scaffold pore shapes and sizes with pore-driven EHT CA and using the minimum value of EHT conductivity that allowed electrical wave propagation in the entire EHT-myocardial tissue. In the second group (G2), we tested different pore shapes with an equivalent area of 0.4 mm^2, but this time the EHT conductivity was increased by adding an offset of 40% of that in healthy tissue. In the third group (G3), we tested completely random, parallel and perpendicular CA in the EHT with respect to the epicardial CMs and we also varied the conductivity to be 10%, 40% and 80% of that in the healthy tissue.

2.2.5. Electrophysiological simulations

The action potential (AP) models of Paci et al. and O'Hara et al. were used to computationally describe the cellular electrophysiology of ventricular-like hiPSC-CMs [25] and human adult ventricular CMs [26], respectively. Electrical impulse propagation was described using the monodomain model [27], defined by the following reaction–diffusion partial differential equation and Neumann boundary condition:

$$\begin{aligned} \partial V / \partial t &= \boldsymbol{\nabla} \cdot (\boldsymbol{D}\boldsymbol{\nabla}V) - I_{ion}(V)/C && \text{in } \Omega \\ \boldsymbol{n} \cdot (\boldsymbol{D}\boldsymbol{\nabla}V) &= 0 && \text{in } \partial\Omega \end{aligned} \tag{1}$$

where V is the transmembrane voltage and I_{ion} is the total current, including all ionic currents and the stimulus current. C is the membrane capacitance, $\boldsymbol{D}$ is the diffusion tensor, Ω is the cardiac domain and $\partial\Omega$ is the boundary of Ω.

Strang's operator splitting method was used to decouple the reaction and diffusion terms [28]. The numerical time integration was implemented using a dual adaptive time integration algorithm [23] in which the reaction and diffusion terms were computed explicitly using the forward Euler method and the value of the time integration step Δt was dynamically selected to guarantee stability. The spatial derivatives in Eq. (1) were numerically integrated using the Finite Element Method. The in-house developed software *ELECTRA* was used for numerical computations [29,30]. All simulations were performed in a personal computer equipped with an Intel® Core® i7-9700K microprocessor clocked at 3.6 GHz and with 32 GB of RAM.

After initializing the models to steady-state, each simulation consisted of three 1 Hz-paced cycles, with the last cycle being used for electrophysiological evaluation. The hyperpolarization-activated cyclic nucleotide-gated funny current (I_f) in the Paci model was inhibited in the simulations of *in vitro*-based EHT models so that the APs in the EHT were elicited by the applied external stimulation, which has been observed to occur more likely than self-driven EHT depolarization in OM experiments and once the EHT has been engrafted on the myocardial tissue [31]. In simulations of EHTs not coupled to myocardial tissue, stimuli of 5-nA magnitude and 2-ms duration were applied to depolarize the EHT. In simulations of coupled EHT-myocardial tissue, stimuli of 80-mA magnitude and 1-ms duration were applied to the healthy myocardium.

For *in silico* EHTs reproducing *in vitro* results of square and hexagonal pore-shaped EHTs, node sets were defined following the experimental AT-based classification, as described in Section 2.1.2 and depicted in Fig. 2(c). The stimulus current was applied onto the node set initiating the depolarization (i.e. with the shortest AT), shown in red in the figure. In all other simulations with *in silico* EHTs not based on *in vitro* results, the stimulus was applied onto a half millimeter side of the EHT or EHT-myocardial model covering their entire cross sections.

2.2.6. Computation of electrophysiological markers

Numerically computed transmembrane voltage was saved with a time step resolution of 1 ms. AT, AP duration at 90% repolarization (APD$_{90}$), RT and RTG were computed for each node in the EHT or coupled EHT-myocardium meshes. Mean CV was computed on the overall EHT.

In brief, AT was calculated as the difference between a fixed time reference and the time instant when the AP upstroke crossed 0 mV,
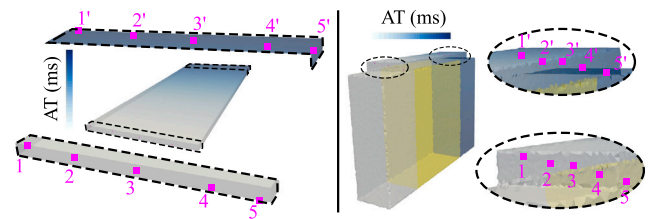

Fig. 5. The five linear paths used for computing the mean EHT CV are depicted for the individual (left) and on MI slab-engrafted (right) EHT. Each path is the line between X and X' with $X = 1, 2, 3, 4, 5$. The yellow area depicts the infarction scar region where the AT was not computed.

i.e. changed from negative to positive values. APD$_{90}$ was defined as the time elapsed from the time instant of maximum voltage derivative in the AP upstroke to the time when repolarization from AP peak to diastolic membrane potential reached 90%. The RT was measured as the sum of AT and APD$_{90}$. To compute RTG, the RTG vector between two nodes was first defined as the ratio of the difference between the two RTs and their Euclidean distance. Next, RTG was calculated for a given node as the mean of the RTG vectors between this node and its neighboring nodes within a radius of 210 μm. This radius value was taken to be the maximum edge length of the coupled EHT-myocardial mesh so that at least one neighboring node was included in all node-wise RTG computations, while avoiding an RTG smoothing effect due to averaging if higher radius values were used. We evaluated RTG only for coupled EHT-myocardial tissue, in which larger repolarization heterogeneities can be expected. In particular, the mean RTG magnitude at the EHT region was analyzed.

For mean CV calculation, we manually selected five nodes in both extremes of the EHT covering the whole thickness as observed in Fig. 5. We calculated the distances and AT differences for the five corresponding linear paths and we computed the ratio between distance and time for defining the path-wise CV values. The mean EHT CV was defined as the mean of these five individual CV values. In Section 3, relative EHT CVs are shown. The reference CV was set to the CV of the EHT with the largest square pore shape, when CA and conductivity were pore-driven, and to the EHT with hiPSC-CMs perpendicularly-aligned and with 10% relative conductivity, when CA and conductivity were uniform.

3. Results

3.1. In vitro-based calibration of in silico EHT models

Model calibration of experimentally-based EHTs identified LDCs leading to simulated activation patterns and maximum AT values closely reproducing the corresponding experimental ones. The experimental AT maps served as a basis to generate *in silico* EHT models that reproduced such maps. The CA in the *in silico* models was defined based on the experimental observations and, next, the LDC value was set so that simulated and experimental maximum ATs matched.

Specifically, simulated and experimental maximum ATs differing by less than 2 ms were obtained employing LDC values ranging from 1.35×10^{-6} to 3.5×10^{-5} cm^2/ms in all tested cases. Fig. 6 depicts examples of experimental and simulated AT maps for square and regular hexagonal pore-shaped scaffolds. Experimentally measured maximum ATs were, in mean, 94 ms for square and 256 ms for hexagonal pore-shaped EHTs, as illustrated in Fig. 6. The delayed activation of the hexagonal architecture was in correspondence to the lower CA (mean 8.11%) and size of this pore shape compared to the square architecture (mean 40.4%). The identified LDC values were, in mean, 1.56×10^{-6} cm^2/ms for hexagons and 1.63×10^{-5} cm^2/ms for squares. Table 2 shows the CAs and LDCs used on the *in silico* experimentally-based EHTs for achieving a maximum simulated AT similar to the

Table 2
Pore shape, CA and LDC values for different experimentally-based *in silico* EHT models to reproduce *in vitro* AT values. S: Square, H: Hexagon and (–): 2D scaffold-free.

Pore shape	–	S	S	S	S	S	S	S	S	S	H	H	H
CA (%)	0	39.3	39.9	46.9	39.5	38.4	40	39.3	40.3	40	8.1	8.3	7.9
LDC (10^{-5} cm^2/ms)	0.35	1	1	1	3.5	2.5	3.5	0.43	1	0.75	0.13	0.2	0.1

(a) Square pore-shaped scaffold.
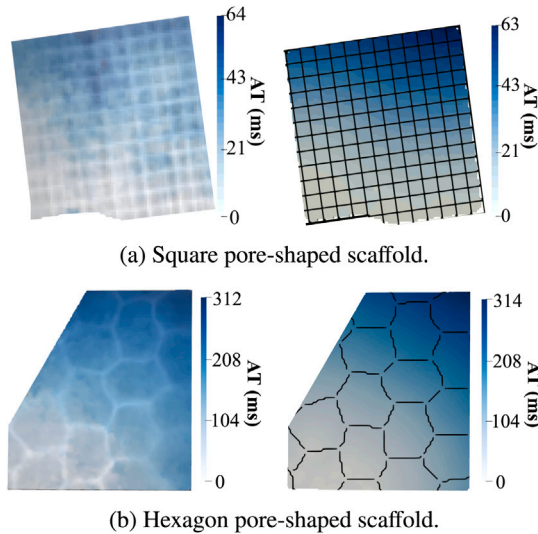

(b) Hexagon pore-shaped scaffold.

Fig. 6. Experimental (left) and simulated (right) AT maps for square (a) and hexagon (b) pore-shaped scaffolds.

experimental case. The fitted linear relationship between CA and LDC was $y = 3.8x + 4.8$, where x is the percentage of CA and y is the LDC in 10^{-7} cm^2/ms.

To sum up, the simulated EHTs replicated the *in vitro* observations and allowed inferring EHT conductivity values, represented as the LDC, in function of the CA.

3.2. In silico assessment of EHT designs

We compared electrical activation for 2D versus 3D scaffold-based EHTs. For this comparison, the 3D EHTs had the same pore geometry and size as the 2D EHTs and presented equal characteristics for all layers along the EHT thickness. Numerical simulations showed that the maximum AT was very similar for the 2D and 3D EHTs. The mean difference in maximum AT over all tested pore geometries was equal to 1.75 ms. In view of these results, subsequent analysis was performed for 3D EHTs only.

Next, we assessed CA for scaffolds with different pore geometries and sizes. Square and rectangle-pore shaped scaffolds presented higher CA than 60° half-angle hexagon pore-shaped scaffolds. The CA increased with hexagon's elongation. Auxetic pore-shaped scaffolds led to the highest CA percentages among all studied designs. Regarding the relationship between CA and pore size, we found a clear inverse relation between them. Fig. 7b summarizes the CA percentages calculated for different pore shapes and sizes.

The maximum ATs and relative CVs for each of the EHTs modeled by varying the pore geometry and size are shown in Fig. 7. The LDC was calculated in each case as a function of the CA percentage presented in Fig. 7b. As can be observed, faster EHT activation was found as the pore size was reduced. Mean maximum AT were of 402, 367.2 and 313.5 ms for the 0.6, 0.4 and 0.2 mm^2 pore size scaffolds over all pore geometries. Similarly, the mean relative CV over all pore shapes increased by 8.32% and 27.3% in the 0.4 and 0.2 mm^2 pore size scaffolds, respectively, when compared with the 0.6 mm^2 pores. Square and rectangle pore-shape scaffolds rendered only slightly different electrical propagation patterns, which were always faster than those for

regular hexagons. As hexagons became more elongated, CA increased, which translated into higher conductivity, leading to lower ATs and higher CVs than for square and rectangle pores. Even though auxetic pores were associated with higher CA, and thus higher LDC, than 30° elongated hexagons, faster propagation of the electrical excitation was observed for the most elongated hexagonal pores. The reason for this is the fact that more fibers were oriented parallel to the depolarizing direction for this pore shape than for auxetic, square and rectangular pore shapes. Fig. 7c shows that the LCA was more than 18% larger for the 30° elongated hexagons than for all other pore geometries. Furthermore, as pore size was reduced, the number of fibers oriented parallel to the propagation wavefront markedly rose for all hexagonal geometries, thus contributing to explain the corresponding increment in CV (Fig. 7d) and reduction in maximum AT (Fig. 7a).

Also, we evaluated the effects of varying the scaffold thickness. Thicknesses of 0.2, 0.4 and 0.6 mm rendered equal activation patterns and a maximum AT of 191 ms as well as equal mean CV of 3 cm/s.

In conclusion, the fastest activation was found for the EHTs with the smallest and most elongated hexagons, which better reproduced cardiac anisotropy. The EHT thickness played a secondary role.

3.3. In silico analysis of the interaction between EHT and infarcted tissue

3.3.1. Role of scaffold pore shape and size in the EHT-myocardium interaction

The EHT models obtained by varying the scaffold's pore shape and size were engrafted on a tissue slab containing healthy and infarcted tissue. To avoid conduction block, we added an offset equivalent to 5% of the healthy myocardial electrical conductivity to the EHT conductivity obtained from the CA-conductivity relationship computed in Section 3.1 (G1 group of simulations). Maps depicting AT and RTG for an EHT with a 30° hexagon pore of 0.4 mm^2 engrafted on a tissue slab are shown in Figs. 9(a) and 9(b). The maximum AT, relative CV and mean RTG for the simulations using different EHT designs can be seen in Fig. 8.

Rectangular pores led to faster conduction than square pores in the coupled EHT-myocardium, with the relative CV being 5.8% higher for the rectangular than the square pore geometry for 0.2 mm^2 pores. In addition, lower ATs and higher CVs were obtained when the auxetic pore was oriented parallel rather than perpendicular to the depolarization direction. The largest relative CV difference of 8.27% between these two pore orientations was found for the smallest pore size. An increment in CV, and consequently decrease in AT, was measured with hexagonal elongation. The mean over all pore sizes of the relative CV in the EHT-myocardium increased from 2.7% to 12% for the regular and 30° elongated hexagons, respectively. The most elongated hexagons yielded faster conduction than all the other pore geometries, reaching the highest relative CV of 14.8% and the lowest maximum AT of 89 ms for 0.2 mm^2 pores.

Overall, the ATs for the EHT-myocardium were higher for 0.6 than for 0.2 mm^2 pores for all pore geometries. A slightly mean increment in the relative CV of 1.53% and 3.7% was measured when the pore size was reduced from 0.6 to 0.4 and from 0.4 to 0.2 mm^2. Higher variability in the relative CV and maximum AT values was found for the coupled EHT-myocardium when smaller pore sizes were assessed. Maximum relative CV differences of 14.3%, 10.9% and 6.9% were found for 0.2, 0.4 and 0.6 mm^2 pore sizes, respectively, when different pore shapes were tested. This suggested that scaffold pore shapes had larger impact on CV, and consequently on depolarization times, when the pore size was smaller.
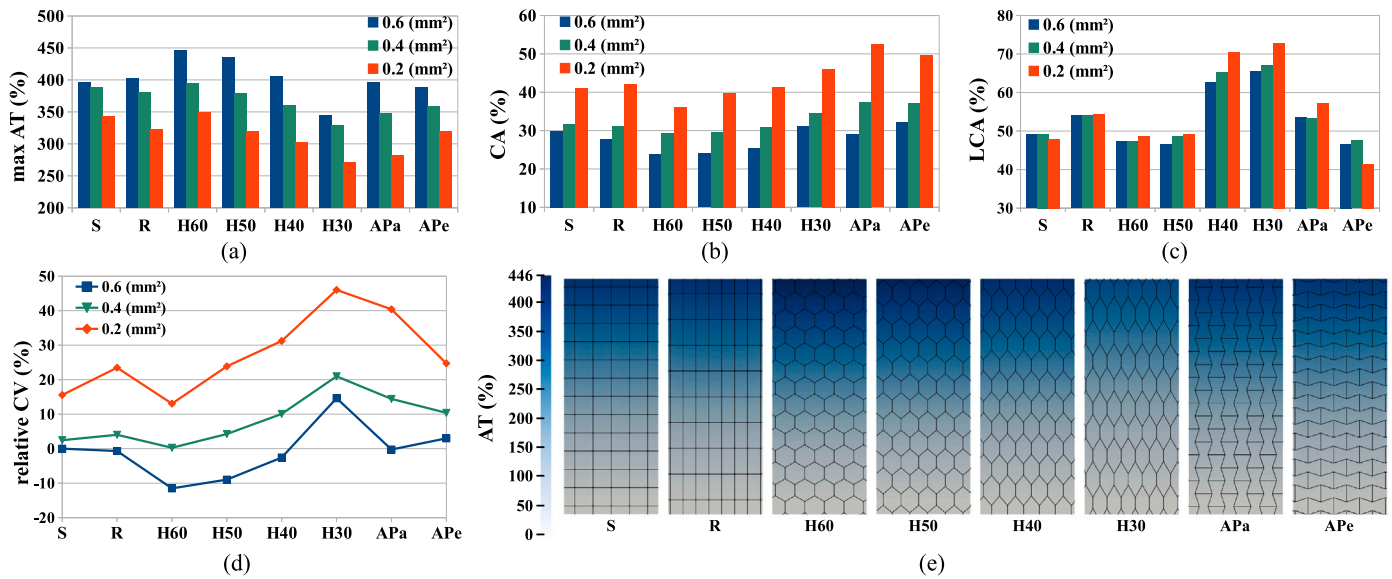
Fig. 7. Maximum ATs, overall CA and LCA and relative CV percentages are shown in (a), (b), (c) and (d), respectively, for 3D EHTs with different scaffold pore shapes and sizes. (e) AT maps for pore geometries with an equivalent pore area of 0.6 mm². S: square, R: rectangular, APa: parallel-oriented auxetic, APe: perpendicular-oriented auxetic and HX: hexagonal with half angle of X degrees.
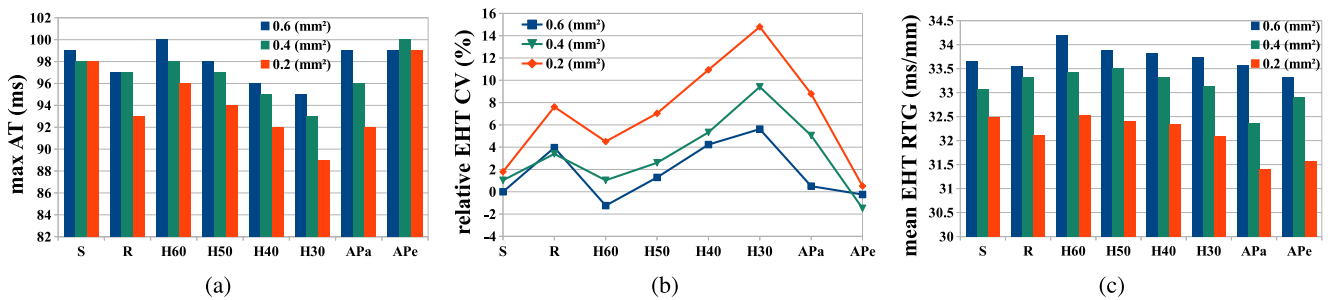

Fig. 8. (a) Maximum AT, (b) relative EHT CV and (c) mean EHT RTG for different scaffold pore shapes and sizes (G1 group of simulations). S: square, R: rectangular, APa: parallel-oriented auxetic, APe: perpendicular-oriented auxetic and HX: hexagonal with half angle of X degrees.

Different pore shapes did not lead to significantly different re-polarization duration in the EHT-myocardium or RTG in the EHT. Differences in the mean RTG over different pore geometries were as low as 1.12, 1.15 and 0.88 ms/mm for 0.2, 0.4 and 0.6 mm² pore sizes, respectively. Thus, the scaffold pore shape played an insignificant role on RTG. The lowest mean RTGs were associated with the auxetic shape aligned with the depolarization direction (see Fig. 8(c)).

The mean RTGs in the EHT were lower for decreasing pore sizes, with mean RTG over all pore shapes decreasing by 0.58 ms/mm for 0.4 with respect to 0.6 mm² pores and by 1.02 ms/mm for 0.2 with respect to 0.4 mm² pores.

3.3.2. Role of EHT conductivity and CA in the EHT-myocardium interaction

Additional groups of simulations (G2 and G3) were conducted to assess the impact of both EHT conductivity and CA on the coupled EHT-myocardium electrophysiology, as described in Section 2.2.4.

For simulations with EHTs having 0.4 mm² pore size and the EHT conductivity being incremented by an offset equivalent to 40% of the healthy myocardium conductivity (G2), the maximum CV increment in the EHT was found for the 30° half-angle hexagonal pore shape (7.6%), as shown in Fig. 10(b). As a consequence, the maximum AT in the EHT-myocardium attained the lowest value of 46 ms for the same pore architecture (see Fig. 10(a)). Similarly to the results reported for *in silico* representations of not engrafted EHTs, the CV in the EHT raised with hexagonal pore elongation (around 2% for elongation step as depicted in Fig. 10(b)).
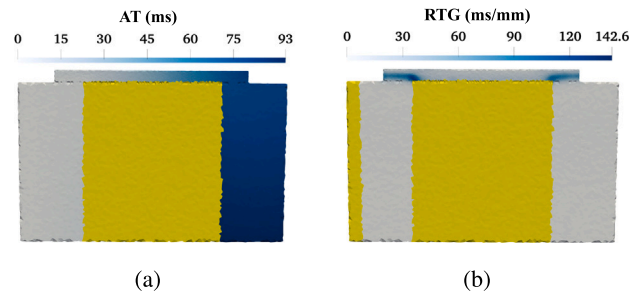

Fig. 9. (a) AT and (b) RTG maps for the most elongated hexagonal pore shape (H30) with a pore size of 0.4 mm². Yellow areas depict tissue regions where the variable of interest was not computed (infarction scar and stimulation region).

When the EHT conductivity and CA were uniform (G3), we observed large variations in the relative CV and maximum AT on the EHT and on the whole EHT-myocardium, respectively. As depicted in Fig. 11(a), the perpendicular CA of the hiPSC-CMs led to total ATs of 109, 62 and 50 ms for 10%, 40% and 80% of EHT conductivity relative to healthy myocardium. For parallel alignment, the total ATs were the lowest, with values of 66, 42 and 36 ms (93.6%, 191.4% and 281% relative CV increments, respectively) for increasingly higher EHT conductivity. Generally, the largest AT reductions and CV increments were found when the relative EHT conductivity increased from 10% to 40%, while
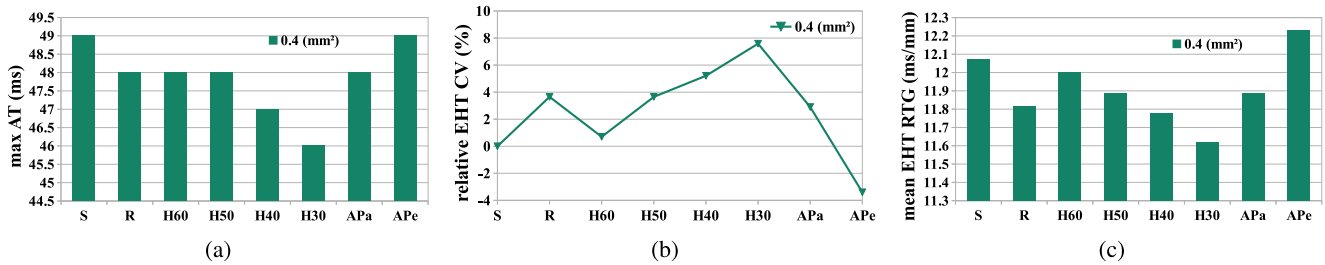
Fig. 10. (a) Maximum AT, (b) relative CV and (c) mean EHT RTG for the G2 group of simulations. EHTs had pore-driven CA and conductivity, 0.4 mm^2 pore size scaffolds were used and the conductivity was incremented by an offset equal to 40% of that in healthy myocardium. S: square, R: rectangular, APa: parallel-oriented auxetic, APe: perpendicular-oriented auxetic and HX: hexagonal with half angle of X degrees.
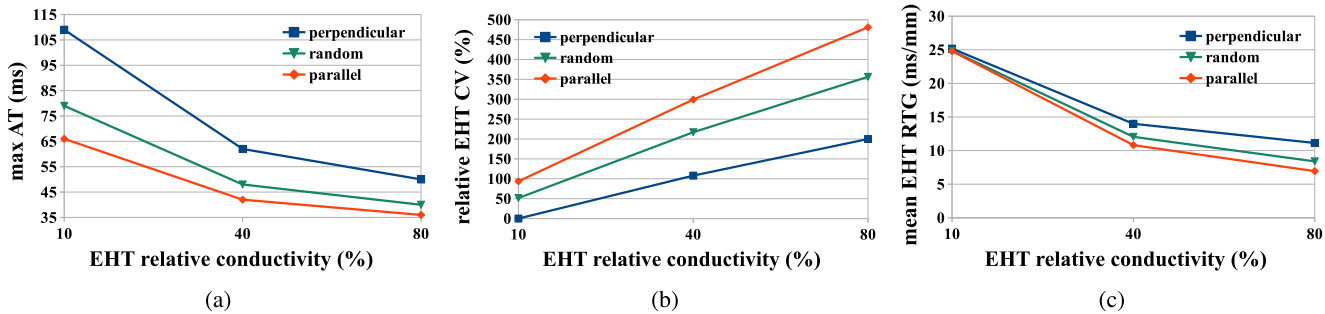

Fig. 11. (a) Maximum AT, (b) relative EHT CV and (c) mean EHT RTG for the G3 group of simulations where EHTs had uniform CA and conductivity. EHTs with conductivity of 10%, 40% and 80% of that in healthy myocardium were evaluated with random, parallel or perpendicular CA with respect to the epicardial cells.

the increase from 40% to 80% led to smaller AT reductions and CV increments, respectively. The differences in maximum AT over the three analyzed alignments were 43, 20 and 14 ms for 10%, 40% and 80% relative EHT conductivity, respectively. While, differences in relative CV over the studied alignments were 93%, 191% and 281% for the three EHT conductivity cases. Then, augmenting the EHT conductivity stressed CV variations in the EHT while it attenuated depolarization times discrepancies in the whole EHT-myocardium due to different CA.

In terms of mean RTG in the EHT after being coupled to the myocardium, we found practically no differences in the values obtained for different pore shapes (differences of 0.61 ms/mm) when the relative EHT conductivity was set to 40% (G2) of that in the healthy myocardium (see Fig. 10(c)). The minimum mean RTG was obtained for the most elongated hexagon, with the value being 11.62 ms/mm, while this slightly increased to 12 ms/mm for regular hexagons.

When the uniform relative EHT conductivity increased (G3), the EHT-myocardial coupling was enhanced in the non-infarcted contact regions and this had an impact on APD$_{90}$. In particular, APD$_{90}$ was increased in the myocardium and was reduced in the EHT within the engraftment region. Fig. 12 illustrates how the repolarization heterogeneities partially vanished with the increment in EHT conductivity. The lowest values of mean EHT RTG were found for the highest EHT conductivity and the parallel orientation of the EHT cells (Fig. 11(c)). We computed mean EHT RTGs of around 25 ms/mm for all EHT alignments when the relative EHT conductivity was 10%. When the relative EHT conductivity was 80%, mean EHT RTGs of 11.13, 8.39 and 6.94 ms/mm were calculated for the perpendicular, random and parallel alignment. The reduction in the mean RTG was more marked when the relative EHT conductivity varied from 10 to 40% than when it varied from 40 to 80%.

In summary, after the EHT being engrafted on the infarcted tissue, EHT conductivities higher than those inferred from *in vitro* experiments were required to enable bi-directional electrical propagation. The hiPSC-CMs conductivity and CA in the EHT, which increased along with cellular maturation, played a major role in increasing CV while reducing RTG, thus contributing to mitigate the arrhythmic risk.
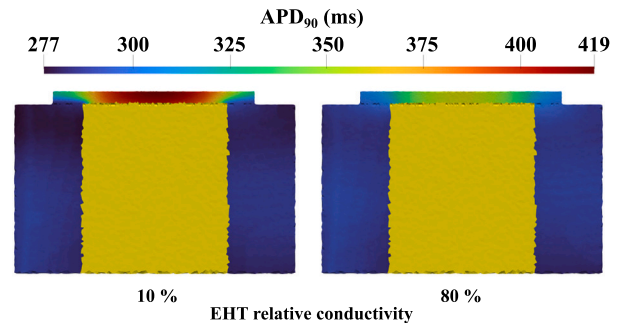

Fig. 12. APD$_{90}$ in the coupled EHT-myocardium is shown for variations in the EHT conductivity when EHT cells were aligned parallel to the epicardial CMs.

4. Discussion

4.1. Calibrated in silico EHT models reproduce in vitro EHT electrophysiology

We acquired and processed OM data from *in vitro* EHTs generated using scaffolds of square and hexagonal pores and we used them to build and calibrate *in silico* EHT models. We aligned the hiPSC-CMs in the models according to their distance to the scaffold walls based on experimental evidence [10,11,17]. Specifically, we followed [17], which reported that hiPSC-CMs located near the pore walls had higher CX43 expression levels than hiPSC-CMs in the pore center and were oriented following the scaffold walls. Here, we represented such CA in the models and we subsequently adjusted the electrical conductivity so that the maximum AT agreed between simulations and experiments.

From the *in vitro* EHT measurements, we observed faster activation and lower scaffold deformation for square pores than for regular hexagonal pores. This might be due to the smaller pore size used in square pore-shaped scaffolds, which incremented the amount of scaffold fibers per unit area, leading to higher CA and reduced pore deformation

due to the raised overall stiffness. As a consequence, cellular coupling was enhanced for square pore-shaped scaffolds with respect to regular hexagonal ones and the electrical propagation was faster, as confirmed by our simulations with the constructed *in silico* EHT models.

In the *in vitro* EHTs used in this study, only the one with hexagonal pore-shape scaffold included 10% hiPSC-CFs cocultured with hiPSC-CMs. Several studies have recently assessed the coculturing of 90% hiPSC-CMs with 10% hiPSC-CFs. Napiwocki et al. [32] observed no significant variation in CV when hiPSC-CFs were added to pre-cultured hiPSC-CMs. Lou et al. [33] demonstrated that the addition of hiPSC-CFs on cultures of hiPSC-CMs, endothelial and smooth muscle cells significantly rose CV. On the other hand, Zhang et al. [34] obtained twice slower electrical conduction when hiPSC-CFs were added to hiPSC-CMs cultures. These contradictory results highlight the uncertainty in the electrophysiological effects of adding hiPSC-CFs. Taking this as a basis, we postulate that the slower electrical activation of our hexagonal pore-shaped EHT could to a large extent be attributed to the pore architecture and size rather than being a reflection of the influence of hiPSC-CFs.

From the experimentally-adjusted relation between LDCs and CA percentage of the analyzed EHTs, we fitted a linear polynomial that allowed to extrapolate the LDC for any other *in silico* EHT built from any scaffold pore shape and size. This was further employed to assess the electrical activity for EHTs with varied scaffold pore shapes and sizes both before and after being engrafted on a transmural slab of infarcted tissue.

4.2. EHTs with scaffolds of small elongated hexagonal pores activate faster than with other scaffold designs

In silico simulations using EHT models showed that, as the scaffold pore size was reduced, a higher number of hiPSC-CMs were in contact with the scaffold walls and this led to higher CA and faster depolarization. Thus, the shortest global AT and highest CV in the EHT was found for the smallest scaffold pore size of 0.2 mm². On the basis of these results, the selection of the 3D printing technique is essential to attain sufficiently small scaffold pores that guarantee rapid electrical propagation in the EHT. The additive manufacturing field is rapidly evolving and more precise structures are expected to be delivered in the coming years.

Regarding scaffold pore shapes, our study emphasized the importance of the CA in the EHT and how this CA varied for different scaffold pore shapes. In cardiac applications, it is vital that the EHT replicates the anisotropy of the native tissue and it renders electrical CV similar to that of healthy myocardial tissue. We observed that auxetic configurations aligned a higher percentage of hiPSC-CMs than other scaffold pore shapes, although the highest CA was not necessarily correspondent with the highest LCA due to the different directions of the scaffold fibers. The scaffolds built with the most elongated (30°) hexagonal pores led to the highest LCA and were the ones best mimicking the cardiac anisotropy of the native tissue and delivering the fastest electrical conduction. Although some works have investigated the performance of scaffolds with pore shapes like auxetic [22,35], rectangular [9], square and hexagonal [10] geometries, to the best of our knowledge this is the first study investigating a large set of scaffold pore geometries and sizes and identifying their suitability in terms of electrophysiological behavior.

Considering our results, EHTs presenting a preferential conduction direction can be best suited for cardiac tissue engineering. Such preferential conduction direction should be taken into account when engrafting the EHT on the infarcted heart. Besides, future computational studies could be conducted to assess the possibility of implanting multiple single-direction conducting EHTs rather than a single EHT depending on the characteristics of the infarction substrates.

4.3. EHT thickness has a negligible electrophysiological role when in vitro

We assessed the role of EHT thickness on electrical activation. Adding printed layers to the scaffold led to EHTs presenting the same electrophysiological behavior, with AT maps sharing similar characteristics for all layers along the different tested thicknesses. This outcome on the very minor role of EHT thickness in electrical terms is in line with results reported in other experimental [22] and computational [24] studies. In [22], similar Ca^{2+} transient signals were experimentally measured from auxetic pore-shaped EHTs with different thicknesses. In [24], the EHT thickness was not a determining factor for electrical activation when the *in silico* EHTs were engrafted on models of partial or transmural infarcted myocardium.

Nevertheless, in an *in silico* study using biventricular infarcted models with engrafted EHTs [31], CV was found to decrease and the arrhythmogenic risk to increase with EHT thickness. In addition, it is paramount to highlight that cellular differentiation improves in 3D constructs but cellular viability decreases with EHT thickness [5,17,22]. Therefore, a trade off in the amount of EHT thickness should be attained to promote *in vitro* cellular differentiation and maturation when in culture while favoring cell viability and integration with the native tissue once the EHT is engrafted on the infarcted cardiac tissue.

4.4. EHT design determines the activation properties of coupled EHT-infarcted myocardium

When the *in silico* EHTs were engrafted on slabs of infarcted tissue, the depolarization wave successfully traveled from the myocardium to the EHT but there was a conduction block when traveling from the EHT to the myocardium. The EHTs showed considerably long ATs with respect to healthy myocardial tissue, in association with conductivity values that were low enough to impair excitation from the EHT to the myocardium due to the presence of a source–sink mismatch [36]. When a conductivity offset equal to 5% of myocardial conductivity was added to the EHT (G1 group of simulations), no conduction block in the coupled EHT-myocardium was observed. This suggests that the current experimental methods to culture hiPSCs in 3D scaffolds should be improved to guarantee that the electrical conductivity in the EHTs is high enough that, when the EHT is engrafted on the infarcted myocardium, propagation occurs between the EHT and the surrounding native tissue.

By designing scaffolds with different pore shapes and sizes, variations in the maximum AT of the coupled EHT-myocardium and in the mean RTG and CV of the EHT were measured. In particular, we observed a reduction in ATs and RTGs and an increment in CV when the pore size was diminished to 0.2 mm² for all tested pore shapes, which is in agreement with the faster conduction we measured experimentally for smaller pore sizes. Similarly to the results reported for the not engrafted EHTs, the most elongated hexagons favored the anisotropic alignment of the hiPSC-CMs in the EHT, thus producing faster conduction in the coupled EHT-myocardium than other scaffold pore shapes. Additionally, the analysis of arrhythmic risk evaluated by the RTG metric showed that, the higher the elongation of the hexagons, the lower the likelihood for arrhythmic activity. Specifically for RTG, we observed that the parallel-oriented auxetic pore shape led to the lowest RTG values, which were somewhat below those of the elongated hexagons. Nevertheless, the variations in RTG over all tested pore shapes were minor.

To complete the characterization of the scaffold design, we set the pore size to 0.4 mm² and we increased the EHT conductivity by adding an offset equal to 40% the healthy tissue conductivity to investigate the impact of the EHT engraftment on the myocardial tissue provided the culturing methods allowed to increase the EHT conductivity (G2 group of simulations). Under those conditions, the maximum AT and the mean RTG were found to attain the lowest values for the 30° half-angle hexagonal pores. Nonetheless, similarly to the outcomes obtained for the G1 group of simulations, the RTG, maximum AT and CV differences for distinct pore shapes were practically negligible.

4.5. Increased EHT conductivity reduces arrhythmic risk in coupled EHT-infarcted myocardium

We further tested variations in the EHT conductivity and alignment of its hiPSC-CMs to assess the impact on the depolarization and repolarization of the coupled EHT-myocardium (G3 group of simulations). We tested EHT conductivity values of 10%, 40% and 80% of that in the healthy myocardium, considering that improved EHT manufacturing and culturing could at some point allow to reach such values. We found that the largest conductivity in the EHT led to drastic exponential-like declines in both AT and RTG while it raised CV linearly. Also, we tested random, parallel and perpendicular hiPSC-CMs alignments with respect to the epicardial cells in the tissue slab and we found that the parallel and perpendicular alignments always produced the lowest and highest AT and RTG, respectively. Taken together, the impact of hiPSC-CMs orientation on EHT-myocardium depolarization was more noticeable for low EHT conductivities, whereas the impact on repolarization heterogeneities and CV was larger for high EHT conductivities. Thus, hiPSC-CMs alignment can be concluded to play a relevant role in mitigating arrhythmic risk throughout the whole maturation process, with the impact on depolarization and repolarization occurring over the whole range of EHT conductivities. These results should be considered when designing scaffolds for regenerative medicine to maximize the benefits on the electrophysiology of the coupled EHT-myocardium.

Our findings on the need for the EHT to present conductivity and CA characteristics that avoid conduction delays are consistent with previous studies [24]. Yu et al. reported that EHT AT and CV were driven by the electrotonic interaction with the healthy myocardium when the EHT engraftment on an *in silico* biventricular model of infarction remuscularization was complete [31]. In a study using two geometries of infarcted left ventricle, Fassina et al. showed how the healthy myocardium drove the EHT activation in the EHT-tissue interacting regions, suggesting that, once the EHT was implanted, the myocardium accelerated the EHT depolarization [37]. Importantly, these results applied to cases where the EHT was electrically coupled to healthy myocardium, whereas, if coupled to the infarct scar, the engrafted EHT preserved its electrophysiological characteristics. Thus, as slow conducting regions favor reentrant arrhythmias [24,31,37], achieving EHT depolarization times and CV values similar to those in healthy tissue should reduce the arrhythmic risk [38]. Our study provides a characterization on how EHT properties, including electrical conductivity and CA modulated by the scaffold shape and size, could help in building EHTs that better mimic the characteristics of healthy myocardial tissue.

With regards to repolarization heterogeneity and proarrhythmic risk, our results describe how the RTG metric is remarkably influenced by the EHT properties. High RTG values are observed when the EHT electrical conductivity is low and/or the hiPSC-CMs in the EHT are not oriented parallel to the epicardial cells of the host myocardial tissue. Laurita et al. [39] experimentally showed that unidirectional blocks developed with repolarization gradients as low as 3.7 ms/mm when an isthmus was present in the cardiac tissue. They predicted that even in absence of isthmuses, unidirectional blocks can occur when repolarization gradients are large. Fassina et al. conducted an *in silico* analysis [24] and reported mean RTGs higher than the threshold set by Laurita et al. [39] for cases in which the conductivities in the EHT and the myocardium were highly distinct. Also, Riebel et al. [40] *in silico* demonstrated that an increase in repolarization heterogeneities due to the injection of a high number of hiPSC-CMs in the infarcted region can lead to enhanced arrhythmic vulnerability. In line with these results, here we found that the major reduction in RTG towards values found in healthy myocardium was attained when the relative EHT conductivity was increased to almost 100%. The addition of electrically conductive elements, as suggested in some studies, could be used to increase the EHT conductivity [35,41]. Furthermore, in accordance with the computational and experimental results in [24,42], we measured higher

APD_{90} values in the healthy myocardium near the engraftment and lower APD_{90} values in the EHT when the conductivity in the EHT was augmented, which confirms better integration of the EHT in the native tissue. It should be noted that in our study the highest RTG values were measured in the EHT, as conductivities lower than the one in the healthy myocardium were always considered. In agreement with this, Fassina et al. reported that, when the EHT conductivity was increased over the one in the healthy myocardium, the electrotonic load applied onto the myocardium by the EHT rose, originating the highest RTGs in the host tissue near the engraftment [24].

Even if to a lesser extent, the contribution of the completely parallel CA in the EHT aided to reduce RTG and increase CV and, thus, to diminish the arrhythmic risk. These effects could be better appreciated when the EHT conductivity was high enough. The smallest, most elongated hexagonal scaffold pores would facilitate such alignment and would contribute to reduce proarrhythmia in the coupled EHT-myocardium.

5. Limitations and future work

Using computational modeling and simulation based on experimental data, we investigated the impact that the EHT design has on cardiac electrophysiology, both before and after implantation on a slab of infarcted ventricular tissue. Our main objective was to assess the effect that the different EHT design features have on electrical activity, including CV and repolarization heterogeneity. Even though our *in silico* representations were carefully based on experimental results, there are areas for improvement that we address in the following.

In terms of CA modeling, we based our *in silico* modeling and simulation study on available experimental data, including acquired and processed OM recordings and published microscopic data of the EHT [10,11,17]. If newer and more precise experimental data became available, e.g. supporting that hiPSC-CMs may orient parallel to the pore direction with less stiffness to facilitate contraction, these could be easily incorporated into the *in silico* models by defining such alignment of the hiPSC-CMs in the EHT. Furthermore, in our *in silico* EHTs, two different distance thresholds were used for the alignment of the cells depending on their distance to the scaffold walls. The first one, 27 μm, was grounded on experimental data [10,17]. A second distance threshold of 55 μm was used to further compare the EHT electrical activity for different pore geometries. The value of this second threshold was chosen to be slightly higher than the 50 μm mean edge length of the EHT meshes, which is lower than currently used mesh resolutions in cardiac simulations [24,31,37]. The value of such second threshold lies between the distance of 27 μm reported in [10,17] and the approximated 100 μm graphically reported by Cui et al. [11] for the orientation of hiPSC-CMs following the scaffold fibers when located within such distance. New studies could refine and extend the results presented here by using finer EHT meshes and testing different threshold distances for the definition of CA.

As derived from our results, the EHT electrical conductivity is a major factor determining the proarrhythmicity of this tissue engineering therapy. Currently, new manufacturing techniques are continuously being tested for improving EHT conductivity, such as the addition of electrically conductive elements to scaffolds or hydrogels [35,41]. Here, we set a unique electrical conductivity in the whole EHT which was proportional to the CA found for each particular design, as aligned cells near the pore walls showed a more mature electrical phenotype [17]. Even though this CA-conductivity relation was adjusted from experimental outcomes as described, enhanced EHT models can be attained with a more realistic representation, which locally incorporates the spatial distribution of the added electrically conductive elements and/or precisely replicate the local areas of more mature/immature hiPSC-CMs on the EHT.

Concerning cellular population modeling, the *in silico* evaluations of this study consider EHTs containing only one cell type, i.e. hiPSC-CMs. These were based on the available experiments, which contained

hiPSC-CMs only, except for the hexagonal pore-shaped EHT that contained 10% hiPSC-CFs. Further studies could use more extensive *in vitro* data containing CFs and other cell types, like endothelial and smooth muscle cells, to enable more detailed *in silico* modeling representative of the electrical interactions between cell types. The simulation of these interactions could serve to further adjust the scaffold design and deliver even deeper improvements on the EHT fabrication procedure.

We tested the engraftment of the EHT on a 3D tissue slab containing an infarct scar. Our results could be extended to include realistic biventricular geometries and infarct scars. Also, we considered a complete attachment of the EHT on the myocardial tissue while it is likely that air bubbles and poor attachment happen due to several factors, including the effects related to cardiac contraction-relaxation cycles. Some computational investigations have reported that homogeneous partial EHT adhesion strongly impacts the transplantation outcome [31]. Other investigations have suggested that when this partial engraftment is distributed all over the patch, it is sufficient to achieve the results that could be obtained if the attachment was complete [37]. In this regard, Gibbs et al. [43] showed that partial heterogeneous attachment between the host myocardium and the EHT strongly affects the probability of developing ectopic beats from the EHT but only when no other non-EHT pacing was applied to the simulations. Based on this, we postulate that including a certain degree of heterogeneous EHT-myocardium attachment would not remarkably alter the presented simulations results. Nevertheless, further *in silico* evaluations could test the impact of partial heterogeneous interactions on the EHT-heart interface and provide a characterization as a function of the infarction substrate.

To close the gap, the *in silico* predictions on the outcomes of EHT-grafted infarcted hearts should be contrasted with *in vivo* electrophysiological data. Based on this, subsequent extensive *in silico* evaluations of the EHT-heart activity could be conducted to aid in the development of improved cardiac assist devices, which could accelerate their therapeutic implementation whilst avoiding costly and time-consuming experiments aimed at optimizing the scaffold design.

6. Contributions

This work presents an experimentally-guided *in silico* modeling and simulation approach for aiding in the design of EHTs, with the following novel contributions:

- We developed novel methodologies to define *in silico* EHT models with varied architectures based on cutting-edge *in vitro* electrical recordings.
- We conducted an extensive evaluation to elucidate the roles of the scaffold's pore shape, size and thickness, the degree of EHT maturation and the CA within the EHT.
- Using our experimentally-guided EHT models, we assessed the impact of the studied EHT designs on the electrical properties of EHTs engrafted on slabs of infarcted ventricular tissues.
- Our analysis pointed to important design criteria required to mitigate the arrhythmic risk and the conduction block associated with EHT engraftment on the infarcted tissue.

7. Conclusion

We simulated an extensive set of EHT models with varied scaffold pore shapes and sizes. Scaffolds made of small, elongated hexagonal pores led to the fastest conduction, as they conveyed the highest number of cells oriented parallel to the depolarization wavefront. *In silico* engraftment of the EHT on infarcted tissue showed that the EHT conductivity is the most critical parameter to avoid conduction block due to EHT-myocardium source–sink mismatch and to increase conduction velocity and reduce depolarization delays and repolarization heterogeneity, all of which contribute to diminish pro-arrhythmic risk. Also, by aligning the EHT cells parallel to the epicardium of the tissue slab, the risk for proarrhythmia following EHT engraftment was further reduced.

CRediT authorship contribution statement

Ricardo M. Rosales: Conceptualization, Data curation, Formal analysis, Investigation, Methodology, Software, Validation, Visualization, Writing – original draft, Writing – review & editing. **Konstantinos A. Mountris:** Conceptualization, Supervision, Writing – review & editing. **Aida Oliván-Viguera:** Data curation, Writing – review & editing. **María Pérez-Zabalza:** Software, Writing – review & editing. **Gerardo Cedillo-Servin:** Data curation, Writing – review & editing. **Olalla Iglesias-García:** Data curation, Writing – review & editing. **Andrei Hrynevich:** Data curation, Writing – review & editing. **Miguel Castilho:** Data curation, Writing – review & editing. **Jos Malda:** Data curation, Writing – review & editing. **Felipe Prósper:** Funding acquisition, Writing – review & editing. **Manuel Doblaré:** Funding acquisition, Supervision, Writing – review & editing. **Manuel M. Mazo:** Data curation, Funding acquisition, Writing – review & editing. **Esther Pueyo:** Conceptualization, Funding acquisition, Methodology, Supervision, Writing – review & editing.

Declaration of competing interest

The authors declare no conflict of interest.

Acknowledgments

References

[1] Adam Timmis, et al., European society of cardiology: Cardiovascular disease statistics 2021, Eur. Heart J. 43 (2022) 716–799.

[2] Stefan Frantz, Moritz Jens Hundertmark, Jeanette Schulz-Menger, Frank Michael Bengel, Johann Bauersachs, Left ventricular remodelling post-myocardial infarction: Pathophysiology, imaging, and novel therapies, Eur. Heart J. 43 (2022) 2549–2561.

[3] Sanne de Jong, Toon A. B. van Veen, Harold V. M. van Rijen, Jacques M. T. de Bakker, Fibrosis and cardiac arrhythmias, J. Cardiovasc. Pharmacol. 57 (2011) 630–638.

[4] Yimu Zhao, Nicole T. Feric, Nimalan Thavandiran, Sara S. Nunes, Milica Radisic, The role of tissue engineering and biomaterials in cardiac regenerative medicine, Can. J. Cardiol. 30 (2014) 1307–1322.

[5] Jonathan Leor, Yoram Amsalem, Smadar Cohen, Cells, scaffolds, and molecules for myocardial tissue engineering, Pharmacol. Ther. 105 (2005) 151–163.

[6] Morcos A. Awad, Aakash Shah, Bartley P. Griffith, Current status and outcomes in heart transplantation: A narrative review, Rev. Cardiovasc. Med. 23 (2022) 11.

[7] Kacey Ronaldson-Bouchard, Stephen P. Ma, Keith Yeager, Timothy Chen, LouJin Song, Dario Sirabella, Kumi Morikawa, Diogo Teles, Masayuki Yazawa, Gordana Vunjak-Novakovic, Advanced maturation of human cardiac tissue grown from pluripotent stem cells, Nature 556 (2018) 239–243.

[8] Elisa Giacomelli, et al., Human-iPSC-derived cardiac stromal cells enhance maturation in 3D cardiac microtissues and reveal non-cardiomyocyte contributions to heart disease, Cell Stem Cell 26 (2020) 862–879.e11.

[9] Ling Gao, Molly E. Kupfer, Jangwook P. Jung, Libang Yang, Patrick Zhang, Yong Da Sie, Quyen Tran, Visar Ajeti, Brian T. Freeman, Vladimir G. Fast, Paul J. Campagnola, Brenda M. Ogle, Jianyi Zhang, Myocardial tissue engineering with cells derived from human-induced pluripotent stem cells and a native-like, high-resolution, 3-dimensionally printed scaffold, Circ. Res. 120 (2017) 1318–1325.

[10] Miguel Castilho, Alain van Mil, Malachy Maher, Corina H.G. Metz, Gernot Hochleitner, Jürgen Groll, Pieter A. Doevendans, Keita Ito, Joost P.G. Sluijter, Jos Malda, Melt electrowriting allows tailored microstructural and mechanical design of scaffolds to advance functional human myocardial tissue formation, Adv. Funct. Mater. 28 (2018) 1803151.

[11] Haitao Cui, Chengyu Liu, Timothy Esworthy, Yimin Huang, Zu-xi Yu, Xuan Zhou, Hong San, Se-jun Lee, Sung Yun Hann, Manfred Boehm, Muhammad Mohiuddin, John P. Fisher, Lijie G. Zhang, 4D physiologically adaptable cardiac patch: A 4-month in vivo study for the treatment of myocardial infarction, Sci. Adv. 6 (2020) eabb5067.

[12] Nicole Silbernagel, Arlene Körner, Jakob Balitzki, Mona Jaggy, Sarah Bertels, Benjamin Richter, Marc Hippler, Andrea Hellwig, Markus Hecker, Martin Bast-meyer, Nina D. Ullrich, Shaping the heart: Structural and functional maturation of iPSC-cardiomyocytes in 3D-micro-scaffolds, Biomaterials 227 (2020) 119551.

[13] Marleen Kristen, Madison J. Ainsworth, Nino Chirico, Casper F. T. van der Ven, Pieter A. Doevendans, Joost P.G. Sluijter, Jos Malda, Alain van Mil, Miguel Castillo, Fiber scaffold patterning for mending hearts: 3D organization bringing the next step, Adv. Healthc. Mater. 9 (2020) 1900775.

[14] Michelangelo Paci, Jussi T. Koivumäki, Hua Rong Lu, David J. Gallacher, Elisa Passini, Blanca Rodriguez, Comparison of the simulated response of three in silico human stem cell-derived cardiomyocytes models and in vitro data under 15 drug actions, Front. Pharmacol. 12 (2021).

[15] Hardik Joshi, Brajesh Kumar Jha, 2D dynamic analysis of the disturbances in the calcium neuronal model and its implications in neurodegenerative disease, Cogn. Neurodyn. 12 (2022).

[16] Ricardo M. Rosales, Konstantinos A. Mountris, Manuel Doblaré, Manuel M. Mazo, Esther Pueyo, In silico electrophysiological evaluation of scaffold geometries for cardiac tissue engineering, in: 2021 Computing in Cardiology, CinC, Brno, Czech Republic, 2021, pp. 1–4.

[17] Pilar Montero-Calle, María Flandes-Iparraguirre, Konstantinos Mountris, Ana S. de la Nava, Nicolás Laita, Ricardo M. Rosales, Olalla Iglesias-García, Elena M. de Juan-Pardo, Felipe Atienza, María Eugenia Fernández-Santos, Estefanía Peña, Manuel Doblaré, Juan J. Gavira, Francisco Fernández-Avilés, Felipe Prósper, Esther Pueyo, Manuel M. Mazo, Fabrication of human myocardium using multidimensional modelling of engineered tissues, Biofabrication 14 (2022) 045017.

[18] Aida Oliván-Viguera, María Pérez-Zabalza, Laura García-Mendívil, Konstanti-nos A. Mountris, Sofía Orós-Rodrigo, Estel Ramos-Marqués, José María Vallejo-Gil, Pedro Carlos Fresneda-Roldán, Javier Fañanás-Mastral, Manuel Vázquez-Sancho, Marta Matamala-Adell, Fernando Sorribas-Berjón, Javier André Bellido-Morales, Francisco Javier Mancebón-Sierra, Alexánder Sebastián Vaca-Núñez, Carlos Ballester-Cuenca, Miguel Ángel Marigil, Cristina Pastor, Laura Ordovás, Ralf Köhler, Emiliano Diez, Esther Pueyo, Minimally invasive system to reliably characterize ventricular electrophysiology from living donors, Sci. Rep. 10 (2020) 19941.

[19] María Pérez-Zabalza, Emiliano Diez, Julia Rhyins, Konstantinos A. Mountris, José María Vallejo-Gil, Pedro Carlos Fresneda-Roldán, Javier Fañanás-Mastral, Marta Matamala-Adell, Fernando Sorribas-Berjón, Manuel Vázquez-Sancho, Car-los Ballester-Cuenca, Margarita Segovia-Roldán, Aida Oliván-Viguera, Esther Pueyo, Improved methods for processing optical mapping signals from human left ventricular tissues at baseline and following adrenergic stimulation, in: 2020 Computing in Cardiology, CinC, Rimini, Italy, 2020, pp. 1–4.

[20] Stefan Pollnow, Nicolas A. Pilia, Gerald Schwaderlapp, Axel Loewe, Olaf Dössel, Gustavo Lenis, An adaptive spatio-temporal Gaussian filter for processing cardiac optical mapping data, Comput. Biol. Med. 102 (2018) 267–277.

[21] Madison S. Spach, Walter T. Miller, David B. Geselowitz, Roger C. Barr, J. Mailen Kootsey, Edward A. Johnson, The discontinuous nature of propagation in normal canine cardiac muscle. Evidence for recurrent discontinuities of intracellular resistance that affect the membrane currents, Circ. Res. 48 (1981) 39–54.

[22] Olga Brazhkina, Jeong Hun Park, Hyun-Ji Park, Sruti Bheri, Joshua T. Maxwell, Scott J. Hollister, Michael E. Davis, Designing a 3D printing based auxetic cardiac patch with HIPSC-CMs for heart repair, J. Cardiovasc. Dev. Dis. 8 (2021) 172.

[23] Konstantinos A. Mountris, Esther Pueyo, A dual adaptive explicit time integration algorithm for efficiently solving the cardiac monodomain equation, Int. J. Numer. Methods Biomed. Eng. 37 (2021) e3461.

[24] Damiano Fassina, Caroline M. Costa, Stefano Longobardi, Elias Karabelas, Gernot Plank, Sian E. Harding, Steven A. Niederer, Modelling the interaction between stem cells derived cardiomyocytes patches and host myocardium to aid non-arrhythmic engineered heart tissue design, PLoS Comput. Biol. 18 (2022) e1010030.

[25] Michelangelo Paci, Jari Hyttinen, Katriina Aalto-Setälä, Stefano Severi, Compu-tational models of ventricular- and atrial-like human induced pluripotent stem cell derived cardiomyocytes, Ann. Biomed. Eng. 41 (2013) 2334–2348.

[26] Thomas O'Hara, László Virág, András Varró, Yoram Rudy, Simulation of the undiseased human cardiac ventricular action potential: Model formulation and experimental validation, PLoS Comput. Biol. 7 (2011) e1002061.

[27] Mark Potse, Bruno Dubé, Jacques Richer, Alain Vinet, Ramesh M. Gulrajani, A comparison of monodomain and bidomain reaction-diffusion models for action potential propagation in the human heart, IEEE Trans. Biomed. Eng. 53 (2006) 11.

[28] Zhilin Qu, Alan Garfinkel, An advanced algorithm for solving partial differential equation in cardiac conduction, IEEE Trans. Biomed. Eng. 46 (1999) 1166–1168.

[29] Konstantinos A. Mountris, Esther Pueyo, The radial point interpolation mixed collocation method for the solution of transient diffusion problems, Eng. Anal. Bound. Elem. 121 (2020) 207–216.

[30] Konstantinos A. Mountris, Leiting Dong, Yue Guan, Satya N. Atluri, Esther Pueyo, A meshless fragile points method for the solution of the monodomain model for cardiac electrophysiology simulation, J. Comput. Sci. 65 (2022) 101880.

[31] Joseph K. Yu, Jialiu A. Liang, William H. Franceschi, Qinwen Huang, Farhad Pashakhanloo, Eric Sung, Patrick M. Boyle, Natalia A. Trayanova, Assessment of arrhythmia mechanism and burden of the infarcted ventricles following remuscularization with pluripotent stem cell-derived cardiomyocyte patches using patient-derived models, Cardiovasc. Res. 118 (2022) 1247–1261.

[32] Brett N. Napiwocki, et al., Micropattern platform promotes extracellular matrix remodeling by human PSC-derived cardiac fibroblasts and enhances contractility of co-cultured cardiomyocytes, Physiol. Rep. 9 (2021) e15045.

[33] Xi Lou, Yawen Tang, Lei Ye, Danielle Pretorius, Vladimir G. Fast, Asher M. Kahn-Krell, Jue Zhang, Jianhua Zhang, Aijun Qiao, Gangjian Qin, Timothy Kamp, James A. Thomson, Jianyi Zhang, Cardiac muscle patches containing four types of cardiac cells derived from human pluripotent stem cells improve recovery from cardiac injury in mice, Cardiovasc. Res. 119 (2023) 1062–1076.

[34] Jianhua Zhang, Ran Tao, Katherine F. Campbell, Juliana L. Carvalho, Edward C. Ruiz, Gina C. Kim, Eric G. Schmuck, Amish N. Raval, André Monteiro Da Rocha, Todd J. Herron, José Jalife, James A. Thomson, Timothy J. Kamp, Functional cardiac fibroblasts derived from human pluripotent stem cells via second heart field progenitors, Nature Commun. 10 (2019) 2238.

[35] Dinorath Olvera, Mina Sohrabi Molina, Gillian Hendy, Michael G. Mon-aghan, Electroconductive melt electrowritten patches matching the mechanical anisotropy of human myocardium, Adv. Funct. Mater. 30 (2020) 1909880.

[36] Peter Spector, Principles of cardiac electric propagation and their implications for re-entrant arrhythmias, Circ: Arrhythm. Electrophysiol. 6 (2013) 655–661.

[37] Damiano Fassina, Caroline M. Costa, Martin Bishop, Gernot Plank, John Whitaker, Sian E. Harding, Steven A. Niederer, Assessing the arrhythmogenic risk of engineered heart tissue patches through in silico application on infarcted ventricle models, Comput. Biol. Med. 154 (2023) 106550.

[38] Susan A. Thompson, Paul W. Burridge, Elizabeth A. Lipke, Michael Shamblott, Elias T. Zambidis, Leslie Tung, Engraftment of human embryonic stem cell derived cardiomyocytes improves conduction in an arrhythmogenic in vitro model, J. Mol. Cell. Cardiol. 53 (2012) 15–23.

[39] Kenneth R. Laurita, David S. Rosenbaum, Interdependence of modulated disper-sion and tissue structure in the mechanism of unidirectional block, Circ. Res. 87 (2000) 922–928.

[40] Leto L. Riebel, Zhinuo J. Wang, Hector Martinez-Navarro, Cristian Trovato, Jacopo Biasetti, Rafael Sachetto Oliveira, Modelling and simulation reveals density-dependent re-entry risk in the infarcted ventricles after stem cell-derived cardiomyocyte delivery, in: 2022 Computing in Cardiology, CinC, Tampere, Finland, 2022, pp. 1–4.

[41] Kaveh Roshanbinfar, Maria Kolesnik-Gray, Miriam Angeloni, Stefan Schruefer, Maren Fiedler, Dirk W. Schubert, Fulvia Ferrazzi, Vojislav Krstic, Felix B. Engel, Collagen hydrogel containing polyethylenimine-gold nanoparticles for drug release and enhanced beating properties of engineered cardiac tissues, Adv. Healthc. Mater. (2023) 2202408.

[42] Massimiliano Zaniboni, Andrew E. Pollard, Lin Yang, Kenneth W. Spitzer, Beat-to-beat repolarization variability in ventricular myocytes and its suppression by electrical coupling, Am. J. Physiol.-Heart Circ. Physiol. 278 (2000) H677–H687.

[43] Chelsea E. Gibbs, Silvia Marchianó, Kelly Zhang, Xiulan Yang, Charles E. Murry, Patrick M. Boyle, Graft-host coupling changes can lead to engraftment arrhythmia: A computational study, J. Physiol. 601 (2023) 2733–2749.